Showcasing research from Professor Jinlong Gong's laboratory, School of Chemical Engineering and Technology, Tianjin University, Tianjin, China

Tunable syngas production from photocatalytic CO_2 reduction with mitigated charge recombination driven by spatially separated cocatalysts

This paper describes the production of syngas from photocatalytic CO_2 reduction with a tunable CO/H_2 ratio via adjustment of the components and surface structure of CuPt alloys and construction of a TiO_2 mesoporous hollow sphere with spatially separated cocatalysts to promote charge separation. Unlike previously reported cocatalyst-separated hollow structures, we firstly create a reductive outer surface that is suitable for the CO_2 reduction reaction. A high evolution rate of 84.2 μmol h^{-1} g^{-1} for CO and a desirable CO/H_2 ratio of 1 : 2 are achieved. The overall solar energy conversion yield is 0.108%, which is higher than those of traditional oxide and sulfide based catalysts (generally about 0.006–0.042%).

As featured in:

See Jinlong Gong *et al.*, *Chem. Sci.*, 2018, **9**, 5334.

ROYAL SOCIETY OF CHEMISTRY

rsc.li/chemical-science

Registered charity number: 207890

Chemical Science

EDGE ARTICLE

View Article Online
View Journal | View Issue

Cite this: *Chem. Sci.*, 2018, **9**, 5334

Tunable syngas production from photocatalytic CO_2 reduction with mitigated charge recombination driven by spatially separated cocatalysts†

Ang Li,‡ Tuo Wang,‡ Xiaoxia Chang, Zhi-Jian Zhao, Chengcheng Li, Zhiqi Huang, Piaoping Yang, Guangye Zhou and Jinlong Gong *

Received 20th April 2018
Accepted 25th May 2018

DOI: 10.1039/c8sc01812j

rsc.li/chemical-science

Photocatalytic CO_2 reduction represents a sustainable route to generate syngas (the mixture of CO and H_2), which is a key feedstock to produce liquid fuels in industry. Yet this reaction typically suffers from two limitations: unsuitable CO/H_2 ratio and serious charge recombination. This paper describes the production of syngas from photocatalytic CO_2 reduction with a tunable CO/H_2 ratio *via* adjustment of the components and surface structure of CuPt alloys and construction of a TiO_2 mesoporous hollow sphere with spatially separated cocatalysts to promote charge separation. Unlike previously reported cocatalyst-separated hollow structures, we firstly create a reductive outer surface that is suitable for the CO_2 reduction reaction. A high evolution rate of 84.2 μmol h^{-1} g^{-1} for CO and a desirable CO/H_2 ratio of 1 : 2 are achieved. The overall solar energy conversion yield is 0.108%, which is higher than those of traditional oxide and sulfide based catalysts (generally about 0.006–0.042%). Finally, density functional theory calculations and kinetic experiments by replacing H_2O with D_2O reveal that the enhanced activity is mainly determined by the reduction energy of CO* and can be affected by the stability of COOH*.

Introduction

Fossil fuels play a pivotal role in energy supply and production, while such sources are unsustainable because of the finite amounts and the massive emission of CO_2 (the main contributor to the greenhouse effect). Generally, there are two approaches to adjust the concentration of CO_2 in the carbon cycle, including the storage of CO_2 and the conversion of CO_2 to useful chemicals.[1] The photocatalytic CO_2 reduction reaction (CRR) represents a promising approach for CO_2 conversion, where the energy required to drive the uphill reaction directly come from solar irradiation.[2,3] For instance, N-doped carbon@$NiCo_2O_4$ double-shelled nano-boxes and CuO–TiO_{2-x}-N_x hollow nanocubes were used as absorption-enhanced photocatalysts, which can efficiently reduce CO_2 to CH_4 and CO.[4,5] $ZnIn_2S_4$–In_2O_3 nanotubes and TiO_2/graphene hollow structures with mitigated charge recombination were also synthesized for an effective photocatalytic CRR to produce CO and CH_4.[6,7] Typically, the CRR can produce various valuable chemical fuels, among which syngas (synthesis gas, the mixture of CO and H_2) is a critical feedstock to produce synthetic liquid fuels *via* an established industrial process (*e.g.*, Fischer–Tropsch synthesis).[8] However, in industrial processes, unsuitable CO/H_2 ratios often limit the practical applications of synthesis. Thus it is critical to precisely control the CO/H_2 ratio from the photocatalytic CRR. To achieve this goal, appropriate catalysts with suitable chemical composition and surface properties are desired. Furthermore, a fundamental understanding of reaction processes and energetic changes in every elementary step is also significant.[8,9]

Another limitation for the photocatalytic CRR lies in the severe recombination of photo-induced charge carriers (electrons and holes). Many strategies have been developed to solve such an ineluctable problem in photocatalytic reactions. Typically, junctions between different materials,[10,11] phases[12] or crystallographic planes[13] have been constructed to enhance charge separation. However, interfaces between different materials will create recombination centers, which greatly restrict the efficiency of charge separation.[14] Alternatively, the loading of cocatalysts can serve as traps of charges to promote their separation.[14,15] Typically, cocatalysts are particles of metals, metal oxides or sulfides deposited on semiconductors, which can be classified into reduction and oxidation cocatalysts. Metal particles (such as Pt, Ag, and alloys)[13,16,17] often act as reduction cocatalysts and electron shuttles when their Fermi

Key Laboratory for Green Chemical Technology of Ministry of Education, School of Chemical Engineering and Technology, Tianjin University, Collaborative Innovation Center of Chemical Science and Engineering (Tianjin), Weijin Road 92, Tianjin 300072, China. E-mail: jlgong@tju.edu.cn

† Electronic supplementary information (ESI) available. See DOI: 10.1039/c8sc01812j

‡ These authors contributed equally to this work.

level lies below the CB of the semiconductor and above the redox potential of the target reaction. On the other hand, metal oxides or sulfides (MnO_x, PbO_2, PbS *etc.*)[13,18,19] can trap holes and are often used as oxidation cocatalysts. Generally, the co-deposition of both reduction and oxidation cocatalysts can trap electrons and holes separately and improve the reduction and oxidation reactions simultaneously. Nevertheless, the simple addition of cocatalysts with a random distribution may increase the possibility of recombination and lead to severe back reactions.[15] One possible solution is to create a catalyst with spatially separated oxidation (hole traps) and reduction cocatalysts (electron traps) based on hollow structures to facilitate charge separation.[14,17,20–23] For such structures with spatially separated cocatalysts, the overall photocatalytic activity is mainly determined by the properties of the outer surface, because active sites loaded inside will obstruct mass transportation and may cause severe cross reactions.[14,17] However, in most previously reported structures, the outer surfaces are loaded with oxidation cocatalysts,[14,17,20–23] creating oxidative outer surfaces that are only suitable for oxidation reactions.[24] This is because loading oxidation cocatalysts inside uniformly with high dispersion is a great challenge due to the incompatibility between the precursor and template.[14,17,20–23] Therefore, it is urgent to develop a structure with a reductive outer surface suitable for reduction reactions including the CRR.

This paper describes the design and fabrication of a structure with reductive outer surfaces, decorated with spatially separated cocatalysts, where oxidation cocatalysts are uniformly dispersed on inner surfaces, which is efficient for the photocatalytic CRR. Besides, the CO/H_2 ratio can be adjusted in a large range including the desired 1 : 2 by changing the component and properties of reduction cocatalysts.[8,9,25] Specifically, TiO_2 hollow spheres, MnO_x and CuPt alloys act as the main catalysts, oxidation and reduction cocatalysts, respectively, and the final product is denoted as MnO_x@TiO_2@CuPt alloy mesoporous hollow spheres (MTCP-MSs, Fig. 1a). Driven by the spatially separated MnO_x particles and CuPt alloys, holes and electrons will flow in opposite directions (Fig. 1b) to enhance the charge-separation efficiency. When these well-separated electrons reach the surfaces of reduction cocatalysts (CuPt alloy) with optimized Cu content, a high catalytic activity with a desired CO/H_2 ratio will be achieved by adjusting the energy of CO_2 activation and CO* desorption during the photocatalytic CRR, which can be explained by density functional theory (DFT) calculations and kinetic experiments.

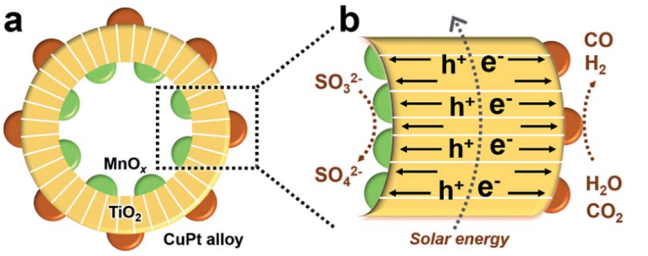

Fig. 1 Schemes of (a) the MTCP-MS structure and (b) the mechanism of the photocatalytic CRR driven by MTCP-MSs. Electrons and holes are induced to opposite directions by spatially separated cocatalysts and the charge separation will be enhanced.

Results and discussion

A hard-templating method (using SiO_2 spheres as templates and dividers to disperse small particles) was used to synthesize the MTCP-MSs.[14,17,26–28] Before the formation of the final structure, the catalysts mainly went through five stages with different morphologies. (1) SiO_2–MnO_x nanospheres (SM-NSs). A modified Stöber method was used to prepare the SiO_2 nanospheres loaded with MnO_x particles.[17] Under alkaline conditions, $KMnO_4$ was chosen as the precursor and it would be slowly reduced by ethanol to form MnO_x (Fig. S2†), ensuring the uniform distribution of MnO_x particles (Fig. 2a, S3 and S1a and b†). The high resolution transmission electron microscopy (HRTEM) image further confirms the existence of MnO_x

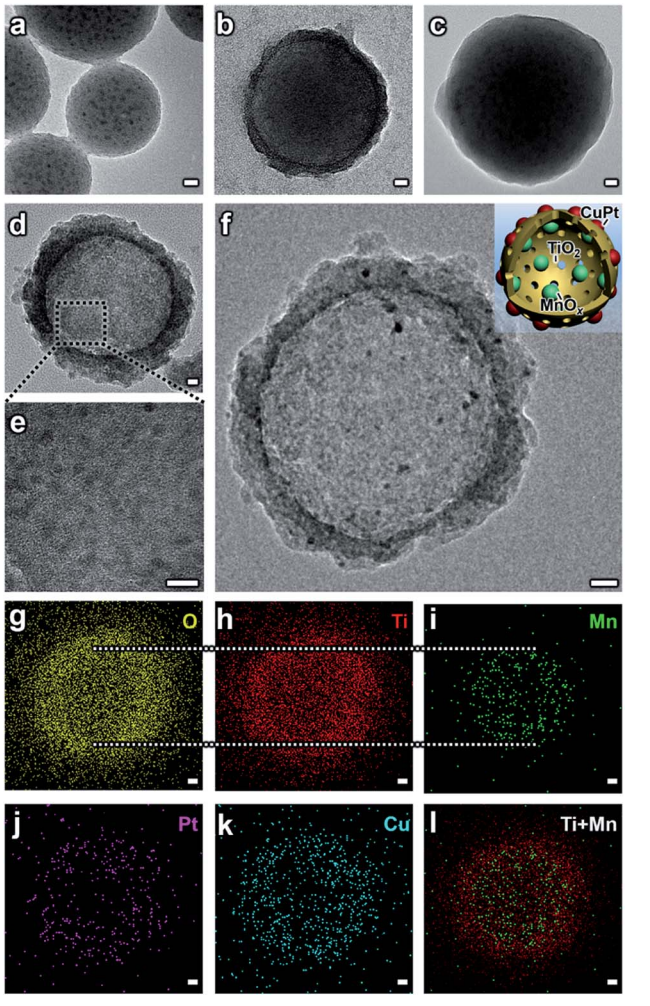

Fig. 2 TEM images of (a) SM-NSs, (b) SMT-NSs, (c) SMTS-NSs, (d, e) MT-MSs and (f) MTCP-MSs. Inset in image (f) is a schematic model of MTCP-MSs. Images (g)– (l) show the EDS mapping of image (f). Corresponding elements are labeled in the upper right corner of every image. Scale bar: 10 nm.

particles (Fig. S3d†). (2) SiO_2–MnO_x@TiO_2 core–shell nanospheres (SMT-NSs). Subsequently, a layer of TiO_2 was uniformly coated on SM-NSs by the hydrolysis of titanium *tert*-butoxide (TBOT) (Fig. 2b and S4†). (3) SiO_2–MnO_x@TiO_2@SiO_2 core–shell nanospheres (SMTS-NSs). Another SiO_2 layer was then coated on the outer surface of SMT-NSs for protection. Without the protective layer, TiO_2 shells would be destroyed during the subsequent calcination step (Fig. S1c†).[26] The smooth surfaces shown in Fig. 2c and S5† suggest the successful coating of SiO_2 layers. Uniformly distributed MnO_x particles can also be observed. (4) MnO_x@TiO_2 mesoporous hollow spheres (MT-MSs). SMT-NSs were then calcined to create a mesoporous structure with a highly crystallized anatase phase (a crystal type of TiO_2 suitable for photocatalysis).[26] Typically, the crystallization processes from amorphous to anatase and from anatase to rutile occur in the temperature ranges of 450–550 °C and 600–700 °C,[26] respectively. Thus the temperature we adopted at 500 °C can ensure the formation of a pure anatase phase, which can also be evidenced by XRD patterns (Fig. S8†). NaOH was used to etch all the SiO_2 layers to form MT-MSs (Fig. 2d and S6†). Uniform MnO_x particles are loaded on TiO_2 shells (Fig. 2e), which could be confirmed by HRTEM (Fig. S6c†). (5) MnO_x@TiO_2@CuPt alloy mesoporous hollow spheres (MTCP-MSs). This final structure was formed after the loading of the CuPt alloy (Fig. 2f). To selectively load CuPt particles uniformly on the outer surface without agglomeration (Fig. S1a†), a photodeposition method (Fig. S7†) was adopted[29] under the protection of a N_2 atmosphere in methanolic solvent, using platinum acetylacetonate and copper acetylacetonate as precursors. Energy dispersive spectroscopy (EDS) mapping (Fig. 2g–l) and HRTEM (Fig. S9a†) exhibit the relative position and components of every material. It is obvious that MnO_x and CuPt particles are selectively loaded on the inner and outer surfaces of TiO_2 hollow spheres. X-Ray Diffraction (XRD) patterns (Fig. S8†) evidenced the formation of TiO_2 and the CuPt alloy. For a low loading and small particle size, the single of MnO_x is not obvious, while can be clearly seen in the HRTEM (Fig. S9a†). The loading of the CuPt alloy can also be evidenced by the result of X-ray photoelectron spectroscopy (XPS), which shows obviously peaks at the banding energies of 74 eV, 71 eV and 932 eV, representing the Pt $4f_{5/2}$, Pt $4f_{7/2}$ and Cu $2p_{3/2}$ of the CuPt alloy (Fig. S10†), matching well with references,[9] indicating the successful loading of the CuPt alloy on the outer surfaces. EDS analysis (Fig. S9b†) focused on a single CuPt particle (within the dotted circle in Fig. S9a†)[30] quantitatively revealed the microscopic composition of the CuPt alloy (Cu : Pt = 3.33), consistent with the result of inductively coupled plasma optical emission spectroscopy (ICP-OES) (Cu : Pt = 3.17). Thus, the catalysts can be finally denoted as $MTC_{3.17}$P-MSs according to the ICP-OES result. HRTEM of $MTC_{3.17}$P-MSs with a higher resolution are provided (Fig. S9†) to show the composition and relative position of the CuPt alloy and MnO_x. By changing the feed ratio of precursors, CuPt alloys with different component ratios were synthesized. The results of EDS at a single point (Cu : Pt = 0.35, 1.48, 8.80) (Fig. S11†) are also consistent with the respective ICP-OES results (Cu : Pt = 0.31, 1.13, 8.72), and the corresponding catalysts can be denoted as $MTC_{0.31}$P-MSs, $MTC_{1.13}$P-MSs and $MTC_{8.72}$P-MSs, respectively.

The Brunauer–Emmett–Teller (BET) surface areas and pore structures of MTCP-MSs were measured by nitrogen adsorption at 77 K. A type IV (defined by IUPAC in 1984 (ref. 31)) isotherm along with two hysteresis loops at relative pressures (P/P_o) of 0.40–0.66 and 0.86–0.99 was observed (Fig. 3a), indicating the presence of mesopores in this sample.[32] The BET surface area was calculated to be about 221.32 $m^2\ g^{-1}$, which can provide abundant catalytically active sites for heterogeneous photocatalysis.[24,33–36] The average pore size was determined to be 4.21 nm, which greatly improves the penetration and transportation of reactants and products.[14,17,27,37–41]

The light absorption for photocatalysts can be characterized by ultraviolet-visible (UV-Vis) spectroscopy (Fig. S12†). The UV-Vis of T-MSs consisted of pure TiO_2 shows a strong absorption within the UV region ($\lambda < 400$ nm) while almost no absorption in the visible region ($\lambda > 400$ nm). For MT-MSs, a slight absorption of visible light can be observed. Furthermore, after the loading of the CuPt alloy to form MTCP-MSs, the absorption of visible light can be greatly enhanced, which may be attributed to the localized surface plasmon resonance of Cu and Pt.[17,42] To further clarify the role of Cu, MT-MSs-Pt was synthesized by loading pure Pt onto MT-MSs *via* photoreduction. Compared with MT-MSs-Pt, MTCP-MSs exhibit stronger absorption of visible light, indicating that the Cu particles could act as a sensitizer to expand the light response of TiO_2 to the visible region.[17,42]

To confirm the enhancement of charge separation and CRR activity by spatially separated cocatalysts ($MTC_{3.17}$P-MSs), reference catalysts including pure TiO_2 mesoporous hollow spheres (T-MSs, Fig. S13†) and TiO_2/MnO_x/$Cu_{3.21}$Pt mesoporous hollow spheres (T/M/$C_{3.21}$P-MSs, Fig. S14†) were also synthesized. T/M/$C_{3.21}$P-MSs stand for T-MSs with MnO_x and CuPt alloys (Cu : Pt = 3.21, detected by ICP-OES) randomly distributed on both inner and outer surfaces, constructed by a direct immersion method.[13] Catalysts with the same components but

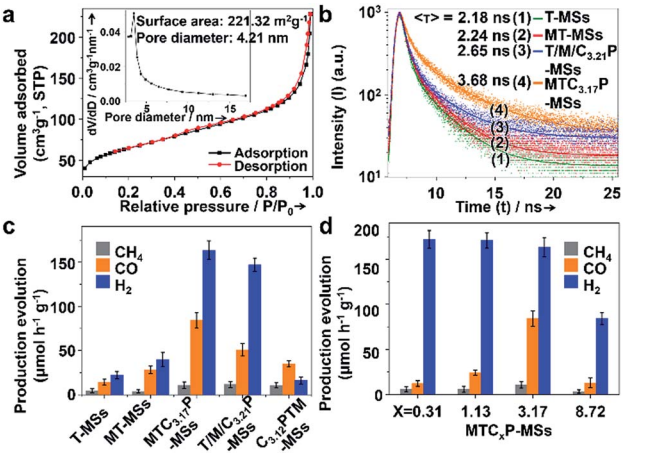

Fig. 3 (a) Nitrogen adsorption isotherms and pore size distribution (inset) of $MTC_{3.17}$P-MSs. (b) TR-PL spectra of different MSs. (c) Gas-evolution rates of MSs with different forms of cocatalyst loading. (d) Gas-evolution rates of different MTCP-MSs with different Cu contents.

oxidative outer surfaces constructed by loading CuPt inside while MnO_x outside were also synthesized, denoted as $C_{3.12}$PTM-MSs. It should be noted that the Cu contents of the CuPt alloy in $MTC_{3.17}$P-MSs (with separated distributed cocatalysts), T/M/$C_{3.21}$P-MSs (with randomly distributed cocatalysts) and $C_{3.12}$PTM-MSs (with oxidation outer surfaces) are all around 76% (molar content). Thus, with similar compositions, the only differences between these catalysts is the distribution of cocatalysts, which should be responsible for the difference of activities.

The charge separation can be monitored by time-resolved photoluminescence (TR-PL) spectroscopy (Fig. 3b). Electrons and holes with long lifetimes would show slow PL decay, indicating efficient charge separation.[14,43–46] The decay curves are obtained by fitting the observed data (the dots in Fig. 3b) according to the extended exponential function[47]

$$I(t) = b + \sum_{i=1}^{n} \alpha_i \exp(-t/\tau_i)$$

where τ_i (excited-state luminescence decay times) and α_i (pre-exponential factors) are the parameters to be fitted, and b is a baseline correction parameter. I and t refer to the instantaneous PL intensity and corresponding time, respectively. The fitting curves are also shown in Fig. 3b. The average decay time, $\langle\tau\rangle$, could be calculated from

$$\langle\tau\rangle = \frac{\sum_{i=1}^{n} \alpha_i {\tau_i}^2}{\sum_{i=1}^{n} \alpha_i \tau_i}$$

The fractional contribution f_i of each decay component was estimated by

$$f_i = \frac{\alpha_i \tau_i}{\sum_{j}^{n} \alpha_j \tau_j}$$

In particular, in our research, to reflect the situation of charge recombination during the reaction, catalysts are dispersed in water and the measurement was performed in air. The samples were excited at 355 nm, and the photoluminescence was monitored at 480 nm. The observed data points are indicated by dots, while the fitting curve are shown as smooth curves in Fig. 3b. The results of fitting parameters such as α and τ are summarized in Table 1.

As shown in Fig. 3b and Table 1, T-MSs exhibit the fastest PL decay (Fig. 3b, curve 1), indicating the most severe charge recombination.[14,43–46] The MT-MSs show a slower PL decay (Fig. 3b, curve 2), suggesting the enhancement of charge separation after the loading of MnO_x. The decay time is further prolonged after the selective loading of the CuPt alloy on the outer surface (Fig. 3b, curve 4), indicating a better inhibition of charge recombination. In addition, T/M/$C_{3.21}$P-MSs (Fig. 3b, curve 3) with randomly distributed cocatalysts show a faster PL decay than $MTC_{3.17}$P-MSs, confirming the critical role of spatial separation of catalysts (Cu contents of T/M/$C_{3.21}$P-MSs and $MTC_{3.17}$P-MSs are very close, and thus the difference between Cu contents is negligible). To further explore charge recombination, steady state fluorescence (PL) spectra were adopted with the wavelength from 280 to 750 nm. The excitation of catalysts with monochromatic light will lead to fluorescence as a result of the recombination of photogenerated charges. Thus, more severe charge recombination will result in stronger fluorescence intensity. The results show that the fluorescence intensity is decreased following the sequence of T-MSs > MT-MSs > T/M/$C_{3.21}$P-MSs > $MTC_{3.17}$P-MSs (Fig. S15†), supporting the conclusion that structures with separated cocatalysts will enhance the charge separation. The enhanced charge separation can be attributed to the spatially separated MnO_x and CuPt alloy, which act as hole and electron traps to drive different charge carriers to flow in different directions. The photocatalytic CRR activity of every catalyst was detected in the solvent of $KHCO_3$ (0.1 M, to enhance the solubility of CO_2) and Na_2SO_3 (0.1 M, acting as a hole sacrificial agent) aqueous solution under AM 1.5G illumination. As a hole sacrificial agent, Na_2SO_3 can rapidly eliminate holes to ensure the smooth proceeding of CO_2 reduction reactions driven by electrons. In the contrastive experiment with the absence of Na_2SO_3 over $MTC_{3.17}$P-MSs, the generation of both CO and H_2 is obviously reduced by about 80% (Fig. S16†), indicating the significant role of Na_2SO_3. The results of the photocatalytic CRR show increased activities (Fig. 3c) following the same trend of increasing charge separation (the trend of activity: $MTC_{3.17}$P-MSs > T/M/$C_{3.21}$P-MSs > MT-

Table 1 Fitting results of the TR-PL spectra of the catalysts[a]

	Pre-exponential factors		Decay life time[b]/ns			Fractional contribution	
Catalysts	α_1	α_2	τ_1	τ_2	$\langle\tau\rangle$	f_1	f_2
T-MSs	0.54	0.46	0.42	2.52	2.18	0.16	0.84
MT-MSs	0.53	0.47	0.46	2.59	2.24	0.17	0.83
T/M/$C_{3.21}$P-MSs	0.52	0.48	0.49	3.03	2.65	0.15	0.85
$MTC_{3.17}$P-MSs	0.35	0.65	0.63	3.94	3.68	0.08	0.92

[a] The double exponential fitting ($n = 2$) was used according to the shape of decay curves. [b] τ_1 and τ_2 are short and long PL lifetimes, respectively. The double exponential PL decay curve suggests that the two recombination processes exist. The fast component of the exponential decay of the TR-PL could be correlated with the band-to-band transition in the high injection regime and the slow component is due to the recombination of minority carriers.[48]

MSs > T-MSs). To reflect the conversion efficiency from solar to chemical energy, the overall conversion yields (η)[49] were supplied based on the generation rate of the product, irradiation intensity of the light source and the change of Gibbs free energy during the reaction (see section 5 of methods in the ESI†). The η values (ref. 49) of $MTC_{3.17}$P-MSs, T/M/$C_{3.21}$P-MSs, MT-MSs and T-MSs are calculated to be 0.108%, 0.065%, 0.036% and 0.018%, respectively, which also coincide with the trend of charge separation. The best η of 0.108% over $MTC_{3.17}$P-MSs is higher than those of general oxide and sulfide based catalysts (generally about 0.006–0.042% (ref. 50 and 51)). Given the similar Cu content (*ca.* 76%) in both structures with separated and randomly loaded cocatalysts, the influence of surface reactions can be ruled out, and thus the enhanced activity can be attributed to the improvement of charge separation. additionally, compared with oxidative outer surfaces ($C_{3.12}$PTM-MSs), reductive outer surfaces ($MTC_{3.17}$P-MSs) show obvious advantages in the photocatalytic CRR (Fig. 3c). During the reaction, the influences of carbon contamination should be ruled out. To verify that carbon in products comes from CO_2 instead of possible carbon containing contaminants, we design a contrastive experiment which was performed without the injection of CO_2 with other situations unchanged over $MTC_{3.17}$P-MSs. The results show that (Fig. S16†) without CO_2 injection, negligible carbon containing products can be detected, indicating that carbon in products originates from CO_2.

The activity and composition of syngas production can also be influenced by the Cu content of the CuPt alloy (Fig. 3d). With a low Cu content ($MTC_{0.31}$P-MSs and $MTC_{1.13}$P-MSs), H_2 is the main product, while the production of CO is low (12.42 μmol h^{-1} g^{-1} and 23.93 μmol h^{-1} g^{-1}, respectively). η values (ref. 49) for $MTC_{0.31}$P-MSs and $MTC_{1.13}$P-MSs are calculated to be 0.016% and 0.031%, respectively. With a high Cu content ($MTC_{8.72}$P-MSs), the catalyst also exhibits relatively low activity for CO (13.16 μmol h^{-1} g^{-1}) with an η of 0.017%. Higher CO activity was achieved with a moderate Cu content ($MTC_{3.17}$P-MSs) (84.18 μmol h^{-1} g^{-1}) with an η of 0.108%. A 0.08 g catalyst was used in the photocatalytic reaction, and the obtained production evolution rate without normalization by catalyst weight shows the same trend over various catalysts (Fig. S17 and Table S1†). The desirable CO/H_2 ratio of 1 : 2 (ref. 8) is also obtained when using $MTC_{3.17}$P-MSs, and it can be concluded that the CO/H_2 ratio can be adjusted in a large range between 1 : 14 and 1 : 2 by changing the Cu content. To investigate the stability of the catalysts, photocatalytic reactions were repeated 4 times under similar conditions within 12 h. The results show that the generation of products decreases by no more than 10% over every catalyst for either CO or H_2 (Fig. S18†), indicating that MTCP-MSs remain stable during the photocatalytic reaction. The morphology of $MTC_{3.17}$P-MSs can also be maintained after the photocatalytic reaction (Fig. S19†). The enhancement of activity and the control of the CO/H_2 ratio are attributed to the balance of every elementary process. With different Cu contents, the surface composition and properties of CuPt cocatalysts are changed, which directly affect the adsorption energy and reaction barrier for all reactants, intermediates and products.[52] Only with an appropriate ratio of Cu/Pt can we obtain the optimal reaction process and achieve the desirable product, which will be elaborately discussed with the help of DFT calculations (see Section 7 of methods in the ESI†).

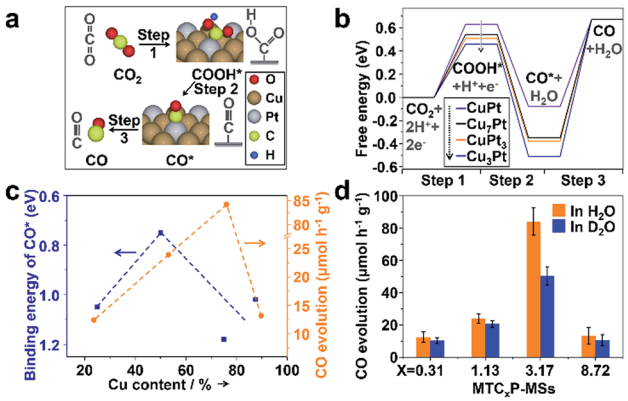

Fig. 4 (a) The main processes and intermediate species for CO_2 reduction to CO. (b) The calculated free energy of the main intermediate species in every step. Models of every steps over each catalyst are shown in Fig. S22.† (c) The calculated binding energy of CO* and the overall activity for CO generation over each catalyst. (d) CO evolution rates of each catalyst in H_2O and D_2O. The rate ratios of $r(H_2O)/r(D_2O)$ over $MTC_{0.31}$P-MSs, $MTC_{1.13}$P-MSs, $MTC_{3.17}$P-MSs and $MTC_{8.72}$P-MSs are 1.20, 1.16, 1.67 and 1.26, respectively, suggesting that the photocatalytic activity over $MTC_{8.72}$P-MSs are greatly affected by D_2O.

The DFT models of CuPt alloys are established based on similar Cu contents ($CuPt_3$, CuPt, Cu_3Pt and Cu_7Pt, respectively) (Fig. S20 and Table S2†). According to previous research,[49,53] the formation of CO from the photocatalytic CRR mainly occurs through the carboxyl process, which can also be proved by the successful detection of adsorbed carboxyl groups (COOH*) during the reaction by using an *in situ* infrared spectrometer (Section 6 of methods in the ESI and Fig. S21†). The carboxyl process can be mainly divided into the following three steps:[49,53] (1) the activation of carbon dioxide ($CO_2 + H^+ + e^- \rightarrow$ COOH*) (Fig. 4a and b), (2) the removal of the hydroxyl radical (COOH* + $H^+ + e^- \rightarrow$ CO* + H_2O, where CO* stands for the adsorbed carbon monoxide) and (3) the desorption of carbon monoxide (CO* → CO). Unlike step 2, steps 1 and 3 are endothermic processes (Fig. 4b), which are thus dominant for the overall activity. Our previous study has shown that the local structure of Pt in the CuPt alloy has a strong effect on the CO* binding strength.[52] With the increase of surface Pt, the binding strength of CO* is weakened, while subsurface Pt behaves oppositely. Additional calculations indicate a similar trend for COOH* adsorption. Genetic algorithm based global optimization indicates that complete Pt skins exist over the CuPt alloy (111) surface until the Pt/Cu ratio is lower than 1 : 1. Thus, the weakest adsorption of CO* and COOH* over Pt sites has been observed on CuPt(111) (a thermodynamically stable facet created by the final calcination during synthesis, which can be observed in Fig. S9a†). Strong CO* binding will inhibit its desorption (step 3)[54] and thus limits the CO formation rate, while too weak binding destabilizes COOH* and thus suppresses the first hydrogenation step (step 1). Therefore,

suitable CO* and COOH* binding strength is needed to achieve the best performance for CO_2 reduction. In addition, DFT shows that the binding energy (defined in Section 7 of methods in the ESI†) of CO on Pt, $CuPt_3$, CuPt, Cu_3Pt and Cu_7Pt is 1.32, 1.05, 0.75, 1.18 and 1.02, respectively, indicating that the adsorption of CO on the CuPt alloy is weakened. Thus, the poisoning of Pt can be weakened by the introduction of Cu. The results of photocatalysis (Fig. 3d) also indicate that increased Cu content will inhibit the competitive H_2 evolution reaction (HER). By investigating the interaction between Cu and Pt based on DFT and XPS, we found that the addition of Cu will enrich the electron density around Pt, which results in a greater energy barrier to inhibit the HER (Fig. S23†).[55–59]

Specifically, with increasing Cu content in our catalysts, the volcano curve of activity is well consistent with the volcano curve of CO* binding energy in Fig. 4c, suggesting that the enhanced activity over the optimal CuPt alloy is mainly caused by the weakening of CO* binding energy. It should be noted that there is a shift of peak positions between the two volcano curves. The shift is mainly caused by the un-uniform distribution of the Pt/Cu ratio in the synthesized nanoparticles, and the influence of COOH* formation. To be more elaborate, a kinetic isotope experiment was performed to investigate the shifted peak position. Interestingly, only $MTC_{3.17}$P-MSs show a notable kinetic isotope effect after replacing H_2O with D_2O (Fig. 4d), indicating that the COOH* formation step influences the whole conversion only over $MTC_{3.17}$P-MSs because hydrogen element only takes part in step 1 instead of step 3, and thus the isotope of hydrogen can only affect step 1. Less stable COOH* was accompanied by weaker binding of CO* (Fig. 4b), consistent with the trend analysis shown in Fig. 4c. Therefore, the different activity is mainly determined by the energy of CO*, which is affected by the stability of COOH*.

Conclusions

In summary, to overcome the main limitations of syngas production by the photocatalytic CRR (unsuitable CO/H_2 ratio and serious charge recombination), we construct a structure with spatially separated cocatalysts and firstly introduced a reductive outer surface to avoid back and cross reactions. The CO/H_2 ratio can be adjusted in a wide range including the desirable 1 : 2 by changing the component of reduction cocatalysts. Furthermore, with the help of DFT calculations and kinetic experiments, we disclose the diversity in activity mainly determined by the energy of CO* desorption and CO_2 activation. Under optimal conditions, the evolution rate of CO reaches 84.2 $\mu mol\ h^{-1}\ g^{-1}$ and the overall conversion yield reaches 0.108%, which is higher than those of traditional oxide and sulfide based catalysts (generally about 0.006–0.042%).[49–51] This work opens up opportunities to develop sustainable and carbon neutral syngas production from the reduction of CO_2 and H_2O using solar energy with rationally designed heterostructures.

Conflicts of interest

There are no conflicts to declare.

Acknowledgements

We acknowledge the National Key R&D Program of China (2016YFB0600901), the National Natural Science Foundation of China (21525626, U1463205, and 21722608), and the Program of Introducing Talents of Discipline to Universities (B06006) for financial support.

Notes and references

1 Y. Fang and X. Wang, *Chem. Commun.*, 2018, **54**, 5674–5687.
2 A. Manzi, T. Simon, C. Sonnleitner, M. Doblinger, R. Wyrwich, O. Stern, J. K. Stolarczyk and J. Feldmann, *J. Am. Chem. Soc.*, 2015, **137**, 14007–14010.
3 G. A. Olah, G. K. Prakash and A. Goeppert, *J. Am. Chem. Soc.*, 2011, **133**, 12881–12898.
4 S. Wang, B. Y. Guan and X. W. Lou, *Energy Environ. Sci.*, 2018, **11**, 306–310.
5 S. I. In, D. D. Vaughn 2nd and R. E. Schaak, *Angew. Chem., Int. Ed.*, 2012, **51**, 3915–3918.
6 S. Wang, B. Y. Guan and X. W. D. Lou, *J. Am. Chem. Soc.*, 2018, **140**, 5037–5040.
7 W. Tu, Y. Zhou, Q. Liu, Z. Tian, J. Gao, X. Chen, H. Zhang, J. Liu and Z. Zou, *Adv. Funct. Mater.*, 2012, **22**, 1215–1221.
8 S. Chu, S. Fan, Y. Wang, D. Rossouw, Y. Wang, G. A. Botton and Z. Mi, *Angew. Chem., Int. Ed.*, 2016, **55**, 14262–14266.
9 X. Zhao, B. Luo, R. Long, C. Wang and Y. Xiong, *J. Mater. Chem. A*, 2015, **3**, 4134–4138.
10 Y. Hou, F. Zuo, A. Dagg and P. Feng, *Nano Lett.*, 2012, **12**, 6464–6473.
11 X. Chang, T. Wang, P. Zhang, J. Zhang, A. Li and J. Gong, *J. Am. Chem. Soc.*, 2015, **137**, 8356–8359.
12 J. Liu, X. Yu, Q. Liu, R. Liu, X. Shang, S. Zhang, W. Li, W. Zheng, G. Zhang, H. Cao and Z. Gu, *Appl. Catal. B Environ.*, 2014, **158–159**, 296–300.
13 R. Li, F. Zhang, D. Wang, J. Yang, M. Li, J. Zhu, X. Zhou, H. Han and C. Li, *Nat. Commun.*, 2013, **4**, 1432.
14 A. Li, X. Chang, Z. Huang, C. Li, Y. Wei, L. Zhang, T. Wang and J. Gong, *Angew. Chem., Int. Ed.*, 2016, **55**, 13734–13738.
15 S. Obregón and G. Colón, *Appl. Catal. B Environ.*, 2014, **144**, 775–782.
16 H. Yan, J. Yang, G. Ma, G. Wu, X. Zong, Z. Lei, J. Shi and C. Li, *J. Catal.*, 2009, **266**, 165–168.
17 A. Li, T. Wang, X. Chang, W. Cai, P. Zhang, J. Zhang and J. Gong, *Chem. Sci.*, 2016, **7**, 890–895.
18 L. Huang, X. Wang, J. Yang, G. Liu, J. Han and C. Li, *J. Phys. Chem. C*, 2013, **117**, 11584–11591.
19 Y. Qu and X. Duan, *Chem. Soc. Rev.*, 2013, **42**, 2568–2580.
20 J. Zhang, Z. Yu, Z. Gao, H. Ge, S. Zhao, C. Chen, S. Chen, X. Tong, M. Wang, Z. Zheng and Y. Qin, *Angew. Chem., Int. Ed.*, 2017, **56**, 816–820.
21 D. Zheng, X. N. Cao and X. Wang, *Angew. Chem., Int. Ed.*, 2016, **55**, 11512–11516.
22 D. Wang, T. Hisatomi, T. Takata, C. Pan, M. Katayama, J. Kubota and K. Domen, *Angew. Chem., Int. Ed.*, 2013, **52**, 11252–11256.

23 Z. Wang, W. Wu, Q. Xu, G. Li, S. Liu, X. Jia, Y. Qin and Z. L. Wang, *Nano Energy*, 2017, **38**, 518–525.
24 J. Zhang, T. Wang, X. Chang, A. Li and J. Gong, *Chem. Sci.*, 2016, **7**, 6381–6386.
25 W. Zhu, L. Zhang, P. Yang, X. Chang, H. Dong, A. Li, C. Hu, Z. Huang, Z. J. Zhao and J. Gong, *Small*, 2018, **14**, 1703314.
26 J. B. Joo, Q. Zhang, I. Lee, M. Dahl, F. Zaera and Y. Yin, *Adv. Funct. Mater.*, 2012, **22**, 166–174.
27 A. Li, P. Zhang, X. Chang, W. Cai, T. Wang and J. Gong, *Small*, 2015, **11**, 1892–1899.
28 X. Wang, Y. Zhao, K. Mølhave and H. Sun, *Nanomaterials*, 2017, **7**, 382.
29 S. Farsinezhad, H. Sharma and K. Shankar, *Phys. Chem. Chem. Phys.*, 2015, **17**, 29723–29733.
30 Z. Luo, C. Li, S. Liu, T. Wang and J. Gong, *Chem. Sci.*, 2017, **8**, 91–100.
31 K. S. Sing, *Pure Appl. Chem.*, 1985, **57**, 603–619.
32 D. Chen, L. Cao, F. Huang, P. Imperia, Y.-B. Cheng and R. A. Caruso, *J. Am. Chem. Soc.*, 2010, **132**, 4438–4444.
33 S. Wang, B. Y. Guan, Y. Lu and X. W. Lou, *J. Am. Chem. Soc.*, 2017, **139**, 17305–17308.
34 C. Li, A. Li, Z. Luo, J. Zhang, X. Chang, Z. Huang, T. Wang and J. Gong, *Angew. Chem., Int. Ed.*, 2017, **56**, 4150–4155.
35 P. Zhang, A. Li and J. Gong, *Particuology*, 2015, **22**, 13–23.
36 S. Wang, C. Li, T. Wang, P. Zhang, A. Li and J. Gong, *J. Mater. Chem. A*, 2014, **2**, 2885.
37 Z. Huang, Y. Liu, Q. Zhang, X. Chang, A. Li, L. Deng, C. Yi, Y. Yang, N. M. Khashab, J. Gong and Z. Nie, *Nat. Commun.*, 2016, **7**, 12147.
38 J. Lu, P. Zhang, A. Li, F. Su, T. Wang, Y. Liu and J. Gong, *Chem. Commun.*, 2013, **49**, 5817–5819.
39 L. Yu, H. Hu, H. B. Wu and X. W. D. Lou, *Adv. Mater.*, 2017, **29**, 1604563.
40 L. Yu, H. B. Wu and X. W. D. Lou, *Acc. Chem. Res.*, 2017, **50**, 293–301.
41 S. Wang, B. Y. Guan, L. Yu and X. W. D. Lou, *Adv. Mater.*, 2017, **29**, 1702724.
42 A. J. Haes and R. P. Van Duyne, *J. Am. Chem. Soc.*, 2002, **124**, 10596–10604.
43 S. D. Stranks, G. E. Eperon, G. Grancini, C. Menelaou, M. J. Alcocer, T. Leijtens, L. M. Herz, A. Petrozza and H. J. Snaith, *Science*, 2013, **342**, 341–344.
44 J. Zhang, M. Zhang, R. Q. Sun and X. Wang, *Angew. Chem., Int. Ed.*, 2012, **51**, 10145–10149.
45 G. E. Eperon, S. D. Stranks, C. Menelaou, M. B. Johnston, L. M. Herz and H. J. Snaith, *Energy Environ. Sci.*, 2014, **7**, 982–988.
46 L. Liu, Z. Ji, W. Zou, X. Gu, Y. Deng, F. Gao, C. Tang and L. Dong, *ACS Catal.*, 2013, **3**, 2052–2061.
47 K. Das and S. De, *J. Lumin.*, 2009, **129**, 1015–1022.
48 S. Shirakata and T. Nakada, *Thin Solid Films*, 2007, **515**, 6151–6154.
49 X. Jiao, X. Li, X. Jin, Y. Sun, J. Xu, L. Liang, H. Ju, J. Zhu, Y. Pan, W. Yan, Y. Lin and Y. Xie, *J. Am. Chem. Soc.*, 2017, **139**, 18044–18051.
50 L. Liu, C. Zhao, D. Pitts, H. Zhao and Y. Li, *Catal. Sci. Technol.*, 2014, **4**, 1539–1546.
51 L. Liu, C. Zhao and Y. Li, *J. Phys. Chem. C*, 2012, **116**, 7904–7912.
52 Z. J. Zhao, R. Mu, X. Wang and J. Gong, *Langmuir*, 2017, **33**, 8700–8706.
53 S. Kattel, W. Yu, X. Yang, B. Yan, Y. Huang, W. Wan, P. Liu and J. G. Chen, *Angew. Chem., Int. Ed.*, 2016, **55**, 7968–7973.
54 J. Liu, F. R. Lucci, M. Yang, S. Lee, M. D. Marcinkowski, A. J. Therrien, C. T. Williams, E. C. Sykes and M. Flytzani-Stephanopoulos, *J. Am. Chem. Soc.*, 2016, **138**, 6396–6399.
55 Z. W. Seh, J. Kibsgaard, C. F. Dickens, I. Chorkendorff, J. K. Norskov and T. F. Jaramillo, *Science*, 2017, 355.
56 S. Zhang, P. Kang and T. J. Meyer, *J. Am. Chem. Soc.*, 2014, **136**, 1734–1737.
57 A. J. Medford, A. C. Lausche, F. Abild-Pedersen, B. Temel, N. C. Schjødt, J. K. Nørskov and F. Studt, *Top. Catal.*, 2013, **57**, 135–142.
58 M. D. Marcinkowski, M. T. Darby, J. Liu, J. M. Wimble, F. R. Lucci, S. Lee, A. Michaelides, M. Flytzani-Stephanopoulos, M. Stamatakis and E. C. H. Sykes, *Nat. Chem.*, 2018, **10**, 325–332.
59 Z. Chen, Y. Song, J. Cai, X. Zheng, D. Han, Y. Wu, Y. Zang, S. Niu, Y. Liu, J. Zhu, X. Liu and G. Wang, *Angew. Chem., Int. Ed.*, 2018, **57**, 5076–5080.